The Performance of Relative Height Metrics for Estimation of Forest Above-Ground Biomass Using *L*- and *X*-Bands TomoSAR Data

Haoyang Yu and Zhongjun Zhang

***Abstract*—Both synthetic aperture radar tomography (TomoSAR) profiles and light detection and ranging (LiDAR) waveforms are the responses of a 3-D canopy structure. Relative height (RH) metrics are extensively applied for forest biophysical parameters [i.e., the forest height and above-ground biomass (AGB)] estimation in full-waveform LiDAR studies. However, the use of RH metrics to forest biophysical estimation with TomoSAR profiles is limited due to the estimation error in the ground peak. To overcome this problem, RH metrics were redefined to avoid directly estimating the ground peak in this article. The redefined RH metrics were examined based on the *L*- and *X*-bands multibaseline (MB) SAR data simulated by LandSAR, which was a coherent backscattering model of 3-D forest canopies with the capability of MB data simulation at a landscape scale. First, the performance of LandSAR in modeling the tomographic features was verified over mountainous areas using the reference DSM and LiDAR digital terrain model acquired in 2012 in the frame of the Daxinganling campaign. Subsequently, the tomographic profiles were retrieved from the simulated MB data by using the Capon method. Additionally, redefined RH metrics were derived and then applied for retrieving the forest height. The highest performance corresponded to the combination of the *L*-band redefined RH metrics, with a correlation of $R^2 = 0.863$. The *X*-band redefined RH metrics performed worst due to limited penetration. Finally, the estimated forest height was used for the AGB retrieval with a height-to-biomass allometry. The R^2 and root-mean-square error of the forest AGB estimated using the combined model were 0.814 and 28.566 t/ha, respectively, compared with the reference forest AGB. All findings demonstrated that the redefined RH metrics had the potential of forest height and AGB retrieval using low frequencies TomoSAR data.**

***Index Terms*—Forest height and above-ground biomass (AGB) retrieval, land synthetic aperture radar (SAR), relative height (RH) metrics, tomoSAR data simulation.**

I. Introduction

FOREST above-ground biomass (AGB) is a key parameter that is correlated with carbon storage [1]. Nevertheless, it is difficult to accurately quantify the global forest AGB owing to the lack of *in situ* measurements on forest plots across different scales [2]. Synthetic aperture radar (SAR) can operate in all weather conditions and is thus a reliable remote sensing technique to retrieve the forest AGB at regional to global scales. The radar backscattering represents the coherent superposition of the signals from scatterers at different locations within a resolution cell [3]. However, the estimation of forest AGB using the radar backscattering coefficient is restricted due to the signal saturation [4]. The introduction of a forest structure parameter into the estimation can relieve saturation effects [5]. The SAR tomography (TomoSAR) technique can be used to characterize a 3-D canopy structure transforming a traditional 2-D imaging pattern to 3-D by focusing the multibaseline (MB) acquisitions along the elevation direction. Since its first demonstration [6], many studies have examined the capability of TomoSAR to realize 3-D building reconstruction [7], [8], deformation monitoring [9], [10], subcanopy terrain estimation [11]–[13], and land cover classification [14], [15].

The retrieval of forest AGB is a significant task realized using the TomoSAR technique [16]. In the last two decades, methods to estimate forest AGB based on TomoSAR data have been developed. These methods can be roughly divided into two categories.

The first class of methods uses indicators derived from vertical profiles to directly estimate the forest AGB. These methods first obtain success in tropical forest areas by using *P*-band SAR data [17]. In some studies, the estimated tomographic profile is decomposed into several layers, and the backscatter near the canopy top is employed to derive the AGB. The representative processing flow for these algorithms starts with data pretreatment, which is followed by tomographic profile inversion and topographic compensation, and finally, the AGB is estimated using a log-linear regression model. For example, Minh *et al*. [18] explored the potential of the TomoSAR technique to estimate the AGB in a tropical study area using the *P*-band MB airborne dataset. They first noted that the backscatter from the 30 m layer was greatly correlated with the AGB with a Pearson correlation coefficient r_p and root-mean-square error (RMSE) of 0.84 and 34.5 t/ha, respectively. Subsequently, the researchers verified the findings in two study areas in France through cross validation [19]. In a recent study, Tebaldini *et al*. [20] extended the cross validation to five tropical study areas. Li *et al*. [21] reported that combining the *P*-band backscattering

Manuscript received August 7, 2020; revised October 12, 2020 and November 29, 2020; accepted January 8, 2021. Date of publication January 15, 2021; date of current version January 27, 2021. This work was supported in part by the National Key Research and Development Program of China under Grant 2019YFC1509104 and Grant 2018YFA0605403. *(Corresponding author: Zhongjun Zhang.)*

The authors are with the School of Artificial Intelligence, Beijing Normal University, Beijing 100875, China (e-mail: 201631210009@mail.bnu.edu.cn; zzj@bnu.edu.cn).

Digital Object Identifier 10.1109/JSTARS.2021.3051081

coefficient and layered backscattered power could improve the accuracy of the AGB estimation in boreal forests. In addition to the long-wavelength data, the backscattered power from the *X*-band SAR data is correlated with the forest AGB as well. Khati *et al*. [3] utilized quadpolarization TanDEM-X data to retrieve the AGB in a tropical forest in India and the highest performance was noted to be obtained when considering a 27-m backscatter layer in the HH polarization. The above-mentioned studies are mostly using horizontal structure information to estimate forest AGB. In addition to the layered power, it has been noted by Blomberg *et al*. [22] that the integration of the backscattered power between 10 and 30 m above the ground exhibited a higher correlation with the forest AGB than the backscattering coefficient in the boreal forest. However, for this approach, the threshold to differentiate the ground and forest volume should be re-estimated for different study areas.

The methods in the second category take advantage of vertical profiles to first estimate the forest height, which is later used to retrieve the forest AGB through allometric equations. The work in [23] separated the vertical profile into three parts, namely, the phase center, power loss, and noise parts. The forest height was estimated by ranging the power loss from the height of the scattering-phase center (SPC). The LiDAR CHM was employed to optimize the power loss, thereby facilitating the forest height retrieval. Another typical example for the second class was demonstrated by Caicoya *et al*. [24]. In their study, a forest structure-to-biomass allometric equation was proposed and fine performance was achieved with a correlation corresponding to $R^2 = 0.81$ and RMSE $= 36.30$ t/ha. Light detection and ranging (LiDAR) is of the capability of directly measuring the vertical canopy structure. In recent years, the comparison between LiDAR waveforms and TomoSAR profiles has attracted the attention of study teams because both TomoSAR profiles and LiDAR waveforms are the responses of the 3-D canopy structure [25], [26]. These studies indicate the possibility that the methods used in full-waveform LiDAR studies may be also used in TomoSAR studies. Relative height (RH) metrics are widely used in full-waveform LiDAR studies to retrieve the forest height and AGB [27], [28]. However, differences between LiDAR waveforms and TomoSAR profiles arise when using RH metrics. Accurately identifying the ground peak is very important in the retrieval of forest height and AGB with traditional RH metrics. In LiDAR studies, the ground peak of a waveform is found using the Gaussian decomposition [29] and the lowest peak is assumed to be the ground [30]. RH25, RH50, RH75, and RH100 are defined as the vertical distances between the locations of the 25%, 50%, 75%, and 100% energy, respectively, and that of the ground peak [31]. However, in TomoSAR studies, three factors restrict the estimation accuracy of the ground peak from vertical profiles. The first factor is the sidelobe. Even with the super-resolution imaging method, sidelobes are always present [32]. The second factor is the TomoSAR imaging method. Different estimators lead to vertical profiles with diverse vertical resolutions. Li *et al*. [33] compared the ground estimation accuracies of Capon, Fourier beamforming (FB), and compressive sensing (CS) methods with identified ground peak using the MB SAR data acquired in the TropiSAR 2009 campaign. They found that vertical resolution influenced the performance of the ground height retrieval. The third disturbance is caused by the Gaussian decomposition. As demonstrated by Wang *et al*. [34], the ground peak of waveforms can be successfully recognized when the ground peak is obvious. But when the ground peak is weak, the reliability of the Gaussian decomposition reduces. Therefore, the traditional RH metrics cannot be directly applied to estimate the forest height or AGB using TomoSAR profiles. A feasible operation is to redefine the RH metrics to avoid directly estimating the ground peak.

The goal of this study is to evaluate how far RH metrics can be applied for forest biophysical parameters retrieval using the *L*- and *X*-bands TomoSAR profiles. Vertical profiles are derived from MB SAR data simulated by the LandSAR model [35], which is a coherent backscattering model of 3-D forest canopies and can simulate the MB SAR data over mountainous areas at a landscape scale.

II. Review of LandSAR Model

Due to the influence of the temporal decorrelation, the acquisitions of real spaceborne TomoSAR data are very challenging [36]–[38]. In 1987, Richards *et al*. [39] developed a radar backscattering model to simulate the *L*-band backscattering coefficient. The research team [35], [40]–[45] has given much effort to modify this model to precisely simulate the MB SAR data over mountainous areas on a landscape scale. The improved model was referred to as LandSAR.

LandSAR is a 3-D descriptive model, which uses a series of 3-D voxels to depict the forest and topography scenes. The imaging geometry and backscattering components in the LandSAR model are shown in Fig. 1. The forest scene over the mountainous area is illustrated by a conceptual graph of a profile. The *X*-, *Y*-, and *Z*-axes are the directions of range, azimuth, and elevation, respectively. H, B, θ, and α represent the orbit height of the master sensor, baseline length, incidence angle, and baseline angle, respectively. l_{10} and l_{20} are the nearest ranges for the master and slave sensors. The trunks in the left two trees are located in the neighboring profile, accordingly, they cannot be observed in this profile. Four types of cubic cells are applied to describe the 3-D scene, including the soil, ground surface, trunk, and crown (i.e., conifer and broadleaf) cells.

A conifer or broadleaf cell consists of needles or leaves and branches. The orientations and sizes of the needles or leaves and branches within a crown cell are given by a uniform distribution as did in [43]. The calculation of the scattering matrix for leaves, branches, trunks, and ground surface is summarized in Table I. The forest in LandSAR can be regarded as a number of scatterers characterized by corresponding locations and scattering matrices. The scattering matrices of individual scatterer are incoherently superposed to obtain the scattering matrix of a crown cell as did in [45]. The total backscattering of a resolution cell is calculated by the coherent aggregation of scattering matrices of different cells. Considering the influence of surface roughness, Fresnel reflection coefficients matrix is applied to derive the specular reflection matrix from the ground surface by multiplying an element of $\exp[-2(k_0\,\sigma\cos\theta)^2]$ (where k_0 and σ are the free-space wavenumber and root-mean-square height for

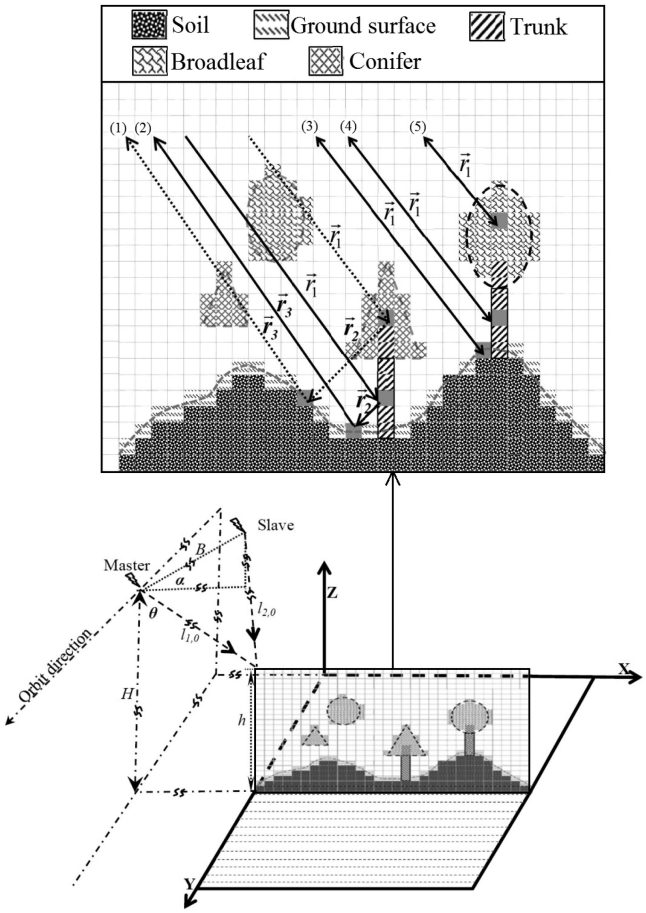

Fig. 1. Imaging geometry and five backscattering elements in the LandSAR model.

TABLE I
CALCULATION OF SCATTERING MATRIX OF SINGLE SCATTERER

Scatterer	Calculation Method
Large disk-shaped leaves	Physical optics approximation [47]
Small leaves or needles	Rayleigh approximation [48]
Branches	Generalized Rayleigh–Gans approximation [49]
Large branches and trunks	Infinite cylinder approximation [42]
Ground surface	Advanced integral equation model [50]

the surface, respectively) [43]. The ray-tracing method is used to calculate the interaction between the electromagnetic wave and different voxels [46].

In LandSAR, five backscattering components are calculated, as shown in Fig. 1, corresponding to the following:

1) double-bounce between the crown and ground cells;
2) double-bounce between the trunk and ground cells;
3) direct backscattering from the ground cells;
4) direct backscattering from the trunk cells; and
5) direct backscattering from the crown cells.

$\vec{r}_1$, $\vec{r}_2$, and $\vec{r}_3$ in Fig. 1 represent the paths of corresponding backscattering elements, respectively. The corresponding backscattering elements are calculated by [51]

$$\vec{E}_{tn}^{sg} = e^{ik_0 l_1}\ \bar{T}_n^t \bar{R}\ \bar{T}_n^r \bar{S}_n^s \bar{T}_n^i \vec{E}_0^i \tag{1}$$

$$\vec{E}_{tn}^{gs} = e^{ik_0 l_1}\ \bar{T}_n^t\ \bar{S}_n^s \bar{T}_n^r \bar{R}\ \bar{T}_n^i \vec{E}_0^i \tag{2}$$

$$\vec{E}_{tn}^{s} = e^{ik_0 l_2}\ \bar{T}_n^t\ \bar{S}_n^s \bar{T}_n^i \vec{E}_0^i \tag{3}$$

where $\vec{E}_{tn}^{sg}$ is the double bounce between the forest and ground cells identifying with backscattering elements (1) and (2). $\vec{E}_{tn}^{gs}$ is the double-bounce between the ground and forest cells and its direction is inverse with $\vec{E}_{tn}^{sg}$. $\vec{E}_{tn}^{s}$ is the direct backscattering for the *n*th forest or ground cell identifying with backscattering elements (3)–(5). $\vec{E}_0^i$ is a unit vector representing the incidence direction and $\bar{R}$ represents the specular reflection matrix of the ground surface. $l_1 = |\vec{r}_1| + |\vec{r}_2| + |\vec{r}_3|$ and $l_2 = 2|\vec{r}_1|$, which are path lengths of the electromagnetic wave in backscattering elements. $\bar{T}_n^t$, $\bar{T}_n^r$, and $\bar{T}_n^i$ indicate the transmissivity matrices in the directions of backscatter, reflection, and incidence, separately. Similar to the models developed by Zeng *et al.* [52]–[54], the LandSAR model extends across frequencies by attenuation as well. As demonstrated by Lin and Sarabandi [55], the transmissivity matrix is applied to express the attenuation with the distance L_n

$$\bar{T}_n = e^{iL_n \begin{bmatrix} \bar{M}_{hh,n} & \bar{M}_{hv,n} \\ \bar{M}_{vh,n} & \bar{M}_{vv,n} \end{bmatrix}} \tag{4}$$

where $\bar{M}_n$ is a matrix concerned with the dielectric constant of scatterers, which can be expressed by [51]

$$\bar{M}_n = \frac{2\pi}{k_0} \sum_{q=1}^{Q_n} \bar{F}_q^s \tag{5}$$

where Q_n is the quantity of scatterers in the *n*th voxel. $\bar{F}_q^s$ represents the forward scattering matrix for the *q*th scatterer in the *n*th voxel, which is derived by the Foldy–Lax approximation [56].

III. DATASET PREPARATION

A. LiDAR Digital Terrain Model (DTM)

The airborne LiDAR point cloud data used in this study were acquired in the frame of the Daxinganling campaign from August 30 to September 14, 2012 [57]. The point density was approximately 2–4 points/m^2. Using the TerraScan software by TerraSolid Ltd., the LiDAR point cloud data were classified into ground, vegetation, and other classes [58]. The LiDAR DTM with a spatial resolution of 1 m was derived from the recognized ground points. The accuracy of the derived DTM is approximately 15 cm along the vertical direction. The elevation of the DTM ranges from 760 to 1163 m, and several steep slopes are distributed in the test site, as shown in Fig. 2(a). The area of the DTM is 9559 $\times$ 8813 m.

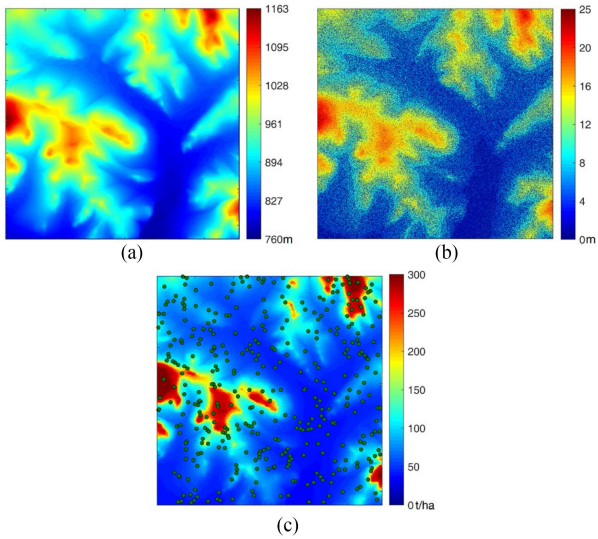

Fig. 2. (a) LiDAR DTM. (b) Simulated CHM. (c) Reference AGB. Green points in (c) indicate the sampling plots to validate the LandSAR model.

B. Simulated Forest Stands and AGB Map

Because the inputs of LandSAR include DTM and 3-D forest scenes, the ZELIG model [59] was used to produce rational forest stands to drive the LandSAR. Due to the different randomized procedures of the ZELIG, it was run 35× to simulate the forest stands from 2 to 200 years in intervals of two years. A total of 94 500 forest stands (35 modeling procedures × 100 successional dynamics × 3 categories of soil moisture: smooth, middle, and rough × 3 categories of ground roughness: dry, middle, and moist × 3 categories of forest species: broad-leaf, conifer, and mixed forests) and 3 368 982 trees were generated using the ZELIG model.

Considering that the area of the simulated forest stands was 30 × 30 m while that of DTM is 9559 × 8813 m, to achieve a more reasonable constitution of a natural 3-D forest scene with a wide dynamic range of the biomass, the locations of forests from simulated stands are reshuffled. First, the preliminary tree location map was generated: the mean interval of the tree location was set as 5 m, and the standard deviation was 5% of the mean interval to avoid a uniform distribution. Then, according to the input DTM, the forest height was determined based on the elevation. It was assumed that trees with a higher height were distributed in the high-elevation areas, while those with a lower height are distributed in low-elevation areas. The CHM and AGB are shown in Fig. 2(b) and (c), respectively. Overall, 395 sampling plots were randomly collected to evaluate LandSAR. The quantities of the sampling plots ranging from 0 to 100, 101 to 200, and 201 to 300 t/ha were 159, 125, and 111, respectively. The locations of the sampling plots are shown in Fig. 2(c), represented by green points.

C. Simulated MB SAR Data

To obtain satisfactory tomographic profiles, the simulated parameters must be reasonably designed considering two factors: the vertical resolution and height of ambiguity (HoA). The former and latter factors depend on the total baseline length and minimum baseline interval, respectively [6]. The parameters for the MB SAR data simulation by the LandSAR model at the *X*- and *L*-bands are listed in Table II. A total of 13 observations were simulated in the *L*- and *X*-bands, respectively. For the *L*-band, the baseline length was increased from 250 to 3000 m in increments of 250 m, whereas the baseline length for the *X*-band was changed from 50 to 600 m in 50 m intervals. Using the simulated parameters, the highest vertical resolution in the *L*- and *X*-bands was 6.84 m and 4.51 m, respectively. To better understand the imaging geometry, the vertical resolution and HoA are used to describe the TomoSAR baselines in the following text.

TABLE II
PARAMETERS APPLIED FOR THE SIMULATION

Parameter	L-band	X-band
Polarization	HH	HH
Sensor height	500 km	500 km
Incidence angle	35°	35°
Baseline length	250 m to 3000 m in intervals of 250 m	50 m to 600 m in intervals of 50 m
Horizontal baseline	216.5 m to 2598.1 m in intervals of 216.5 m	43.3 m to 519.6 m in intervals of 43.3 m
Vertical baseline	125 m to 1500 m in intervals of 125 m	25 m to 300 m in intervals of 25 m
Resolution	5 m	5 m
Wavelength	0.235 m	0.031 m

IV. METHODOLOGY

The process flow to estimate the forest height and AGB by using the RH metrics is displayed in Fig. 3, including the MB data simulation, flat earth phase removal, tomographic profile retrieval using the spectral estimation method, RH metrics extraction, geocoding, forest height estimation, and forest AGB retrieval. The methods to realize the tomographic profile inversion, RH metrics extraction, forest height, and AGB retrieval are introduced in this section.

A. Spectral Estimation Techniques

The estimation of the tomographic profile can be considered to be a spectral estimation problem. Note that different spectral estimators usually generate different distributions of the backscattered power. A recent study [32] compared the capability of different estimators, including the Capon, Fourier FB, and CS approaches, to retrieve the super-resolution backscattered power. Capon is a widely used nonparametric spectral estimator, which demonstrates excellent potential in improving the vertical resolution and this estimator is used to retrieve the tomographic profile in this study.

Generally, the interferometric vertical wavenumber between two observations can be defined as [3]

$$k_Z \cong \frac{4\pi B_\perp}{\lambda R \sin\theta} \tag{6}$$

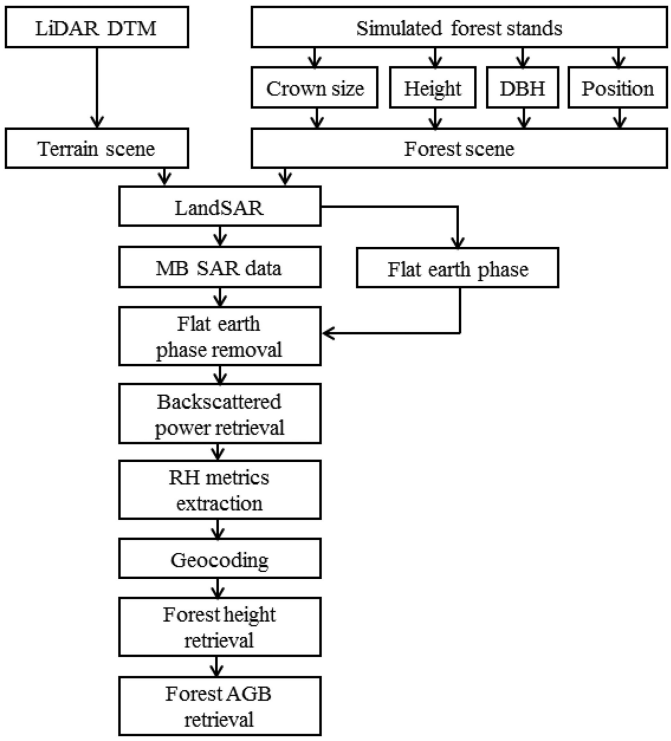

Fig. 3. Process flow to estimate the forest height and AGB using RH metrics.

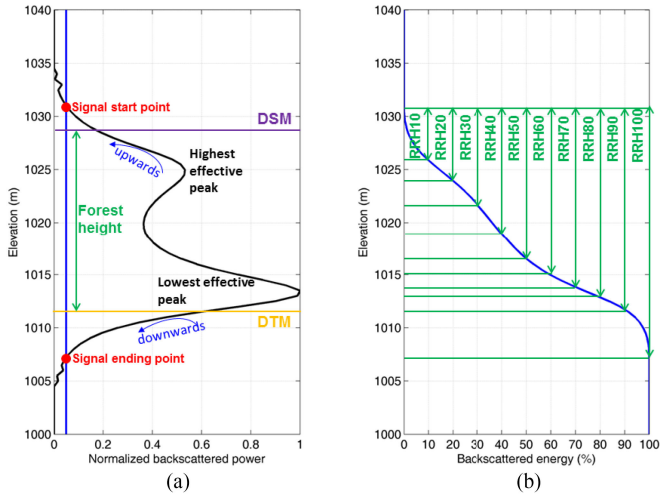

Fig. 4. Schematic view of redefined RH (RRH) metrics. (a) Tomographic profile with sidelobes (i.e., black curve line) and 5% of the power of the maximum effective peak (i.e., blue vertical line). (b) Backscattered energy and RRH metrics (the backscattered energy is calculated from the SSP).

where $B_\perp$ is the perpendicular baseline length, R is the slant range, and θ is the incidence angle. Capon employs the MB covariance matrix to reconstruct the tomographic profile. The power retrieval of Capon can be expressed as [60]

$$P_C(\delta) = \frac{1}{a^H(\delta) C^{-1} a(\delta)} \tag{7}$$

where C is the data covariance matrix and $a(\delta) = [1, \exp(jk_{Z2}\delta), \ldots, \exp(jk_{ZM}\delta)]$ is the steering vector for the corresponding scatter at elevation δ. $()^H$ and $()^{-1}$ denote the transpose conjugate and inversion operators, respectively. The Capon spectral estimator is used to examine the performance of LandSAR in simulating the TomoSAR features and generating the tomographic profiles for the following RH metrics extraction.

B. RH Metrics Extraction

1) Recognition of Effective Lobes: Sidelobes are the primary disturbance in TomoSAR studies and they are determined by the volume coherence, TomoSAR imaging method, and baseline distribution [61]. The following procedure is implemented for the recognition of the real backscattering peaks from sidelobes, as shown in Fig. 4(a). Peaks with the amplitude exceeding 5% of the maximum peak and distributing within a reasonable elevation range (i.e., TanDEM-X DEM - 25 $<$ elevation $<$ TanDEM-X DEM + 10) are regarded as effective peaks (i.e., dominant lobes), while the rest of the peaks are considered as sidelobes. The reasonable elevation range is determined based on the case that TanDEM-X DEM is processed from the *X*-band InSAR data and *X*-band SPCs are mostly distributed near the canopy top instead of the ground surface. Subsequently, beginning from the center of the recognized highest effective peak and moving along the vertical profile upwards, the profile is truncated when the backscattered power reduces to 5% of the power of the maximum effective peak. Finally, beginning from the center of the recognized lowest effective peak and moving along the vertical profile downward, the profile is also truncated when the backscattered power reduces to 5% of the power of the maximum effective peak. The profile distributed between the upper truncated point and the bottom truncated point is the true TomoSAR profile.

The above-mentioned thresholds and elevation range are determined to derive the best performance in this study. These thresholds and reasonable elevation range should be afresh selected for different study areas and TomoSAR data. For example, in the study of Caicoya *et al.* [24], a threshold of 20% of the maximum peak successfully removed the sidelobes and a threshold of 30% was applied to truncate the profile, while in the work of Pardini *et al.* [26], 10% of the maximum peak and elevation range of TanDEM-X DEM - 50 $<$ elevation $<$ TanDEM-X DEM + 20 are used to facilitate identifying the effective lobes.

2) Redefinition of the RH Metrics: The recognition of ground peak is the key when using the conventional RH metrics. RH25, RH50, RH75, and RH100 are defined as the vertical distances between the locations of the 25%, 50%, 75%, and 100% energy, respectively, and that of the ground peak. In the work of Pardini *et al.* [26], RH100 is redefined as the height exceeding the tallest peak at which the backscattered power reduces by an empirical threshold of 3 dB. In this study, another way to define the RH metrics is given to avoid directly estimating the ground peak.

The schematic view of the redefined RH (RRH) metrics is shown in Fig. 4(b). In the RRH metrics, instead of the first and last bins in which the backscattered power exceeds zero,

the upper truncated point and the bottom truncated point are defined as the signal startpoint (SSP) and signal end point (SEP), respectively. The total backscattered energy is calculated based on true TomoSAR profiles derived in Section IV-B1 (i.e., profile distributed between the upper truncated point and the bottom truncated point) by obtaining the integral along the vertical direction, as follows:

$$P_{\text{Energy}} = \int_{\delta=\text{SEP}}^{\delta=\text{SSP}} P_C(\delta)\, d\delta \tag{8}$$

where $P_C(\delta)$ indicates the backscattered power estimated using the Capon method. Based on the fact that the signal below the ground surface should not be caused by the forest structure, the backscattered energy is calculated from the SSP instead of SEP. By considering the SSP as the upper limit of the integration, the backscattered energies at different percentages are calculated. The RRH metrics can be derived considering the vertical distances between the SSP and the location in which the backscattered energy attains the corresponding percentage. In this study, the backscattered energy interval of 10% is used (i.e., the RRHs at energy percentages of 10% to 100% are denoted as RRH10 to RRH100, respectively).

C. Forest Height and AGB Retrieval

The forest height is estimated using a single element of RRH10 to RRH100 and their combinations, depending on the simple linear regression method. The influence of different total baseline lengths (i.e., different vertical resolutions) on the forest height estimation is analyzed. The *L*-band MB SAR datasets simulated with vertical resolutions ranging from 13.68 to 6.84 m and the *X*-band dataset with a vertical resolution of 6.78 m (400 m total baseline length) are used to estimate the forest height. The use of allometry to retrieve forest AGB is restricted by changeable forest stand densities [62], [63]. Because the distribution of forest stand is relatively homogeneous in this study, a height-to-biomass allometry is used in the estimation of forest AGB as [64]

$$\text{AGB} = aH^b \tag{9}$$

where H is the estimated forest height. The models for the forest height and AGB estimation are determined based on 197 samples randomly selected from 395 plots. The estimated forest height and AGB values are used to validate the models, considering the remaining 198 plots. The performance of each model is evaluated using the coefficient of determination R^2 and RMSE between the reference and retrieved forest height and AGB values.

V. Results

A. Simulation Results

The results of the processed MB SAR data are shown in Fig. 5. Fig. 5(a)–(c) shows the *L*-band 2-D SAR intensity and tomographic profiles in areas with forest height ranging from 8 to 13 m and 13 to 21 m along the yellow and red lines shown in Fig. 5(a), respectively, with a vertical resolution of 6.84 m.

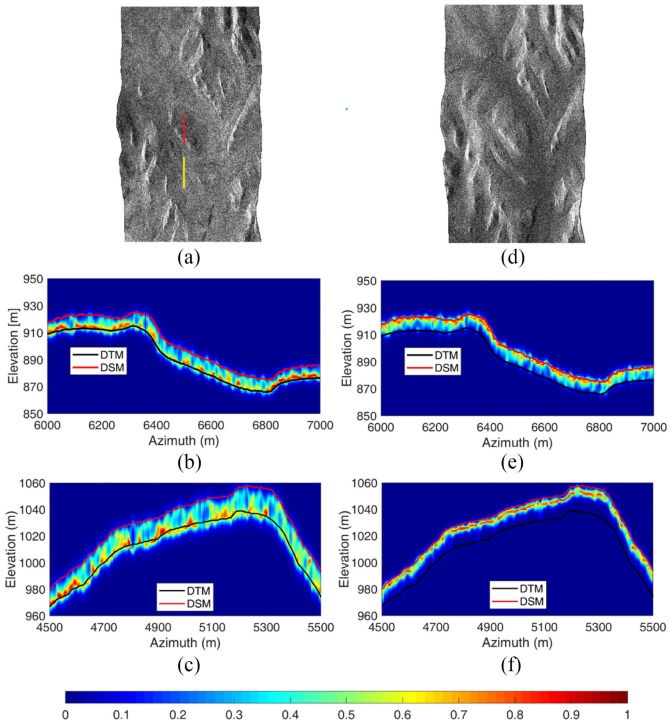

Fig. 5. Simulation results corresponding to the LandSAR. (a) *L*-band 2-D SAR intensity. (b) and (c) *L*-band tomographic profiles in areas with forest height ranging from 8 to 13 m and 13 to 21 m along the yellow and red lines shown in (a), respectively, with a vertical resolution of 6.84 m. (d), (e), and (f) Corresponding results of the *X*-band, with a vertical resolution of 4.51 m. The black and red lines in (b), (c), (e), and (f) represent profiles from the LiDAR DTM and reference DSM, respectively.

The tomographic profiles are normalized between zero and one. Fig. 5(d)–(f) shows the results of the *X*-band corresponding to the conditions in Fig. 5(a)–(c), respectively. Speckle noise can be clearly observed in Fig. 5(a) and (d). The black and red lines in Fig. 5(b), (c), (e), and (f) represent the profiles from the LiDAR DTM and reference DSM, respectively. The distribution of the backscattered power is prominently characterized by LandSAR. As illustrated in Fig. 5(b), (c), (e), and (f), the estimated profiles agree well with the LiDAR DTM and reference DSM (reference DSM = LiDAR DTM + simulated CHM). The results show that the TomoSAR in the *L*-band can penetrate the canopy and reach the ground, and the backscattering contributions from the ground and canopy are well recognized. Moreover, the SPCs of the *L*-band tomographic profiles in the HH polarization are mostly distributed near the ground surface. This phenomenon occurs owing to the dominant effect of the double-bounce backscattering from the crown and ground cells and from the trunk and ground cells. A contrasting phenomenon is observed in the profiles of the *X*-band, and the scattering contributions primarily correspond to the canopy top due to the dominant effect of the volume scattering. In general, the penetration of the *X*-band TomoSAR in the forested areas is determined by the forest height (or scatterer density) [3]. Until a certain forest height, no distribution of the backscattered power can be observed in the canopy bottom, as shown in Fig. 5(f). These phenomena are consistent with the theoretical expectation that the penetration

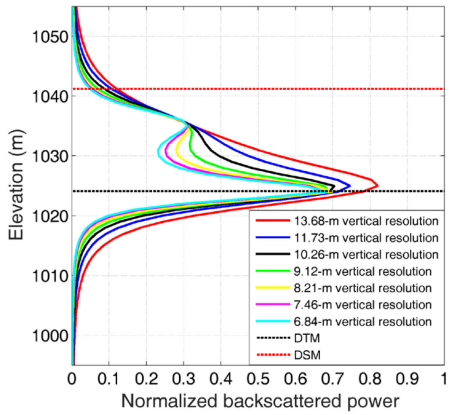

Fig. 6. Changes in the tomographic profiles with the vertical resolutions ranging from 13.68 to 6.84 m, and a fixed HoA of 328.32 m.

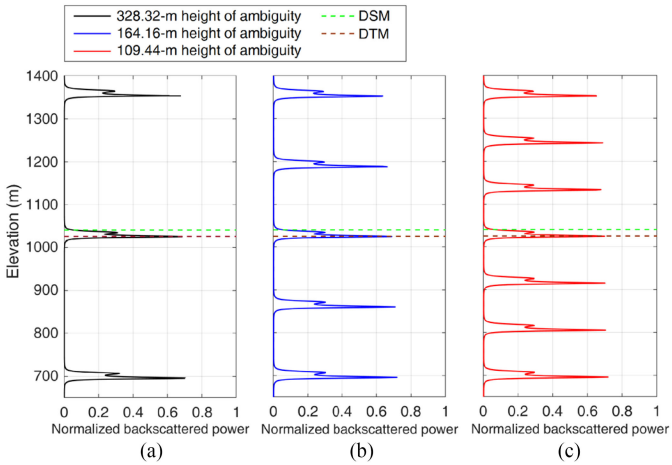

Fig. 7. Changes in the tomographic profile with HoA of (a) 328.32 m, (b) 164.16 m, and (c) 109.44 m and a fixed vertical resolution of 6.84 m.

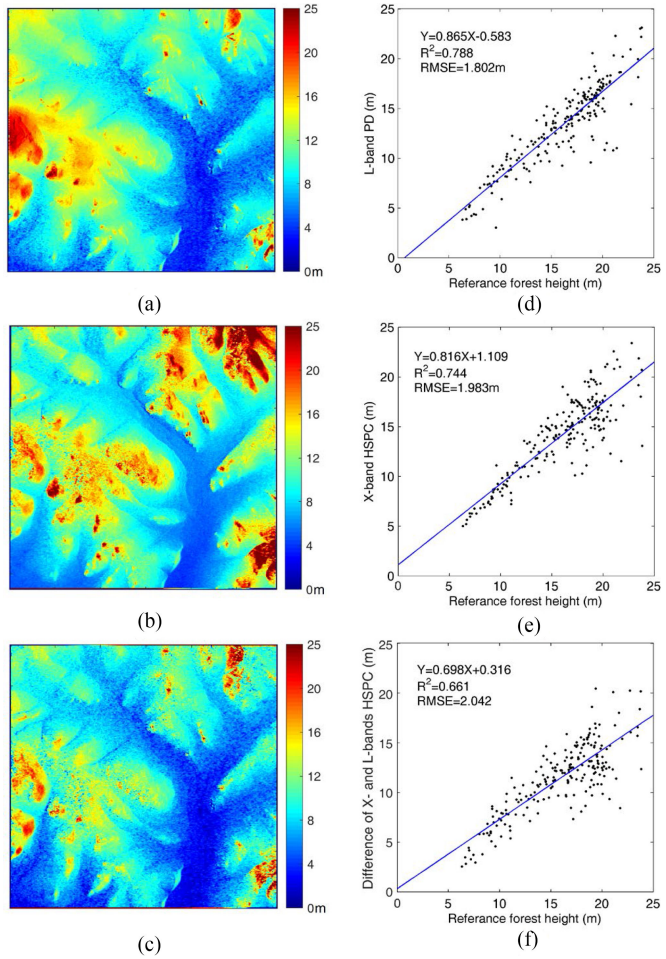

Fig. 8. Sensitivities of the reference CHM and SPC-retrieved indicators with a vertical resolution of 6.84 m and the HoA of 328.32 m for the *L*-band, and with a vertical resolution of 4.51 m and the HoA of 216.55 m for the *X*-band. (a) *L*-band PD. (b) *X*-band HSPC. (c) Difference in the *X*- and *L*-bands SPCs. (d)–(f) Scattering plots of (a)–(c) against the reference CHM, respectively. The blue lines are the linear fitting lines for a given R^2 and the formula.

capability of the SAR microwave of the *L*-band is stronger than that of the *X*-band.

The influence of the vertical resolution and HoA on the tomographic profile estimation was analyzed. Fig. 6 demonstrates the tomographic profiles for a sampling plot derived from the simulated *L*-band MB SAR images, with the vertical resolutions ranging from 13.68 to 6.84 m, and a fixed HoA of 328.32 m. The sampling plot is located at the center of the image. A clear waveform change can be observed as the total baseline length varies, indicating that the number of identified peaks increases as the vertical resolution increases. This phenomenon can be explained by the total baseline length.

Fig. 7 shows the tomographic profiles for the same sampling plot in Fig. 6 derived from the simulated *L*-band MB SAR images, with HoA of 328.32–109.44 m and a fixed vertical resolution of 6.84 m. Different from the results in Fig. 6, the waveforms do not change considerably as the HoA decreases. It can be clearly noted from Fig. 7 that the vertical distance between the real tomographic profile and its repetition increases corresponding to the increased HoA. It can be expected that the HoA decreases as the minimum baseline increment increases.

The height of the SPC (HSPC) (i.e., the height from the SPC to the ground) and penetration depth (PD) can be extracted with the knowledge of DTM and DSM, respectively. Correlations between the reference CHM and SPC-retrieved indicators from the simulated *L*- and *X*-bands MB SAR images are illustrated in Fig. 8. Fig. 8(a)–(c) shows the *L*-band PD, *X*-band HSPC, and the difference in the *L*- and *X*-bands SPCs, respectively. By comparing Fig. 8(a)–(c) with Fig. 2(b), similar features can be noted in the flat as well as the mountainous areas. Fig. 8(d)–(f) shows the scattering plots corresponding to Fig. 8(a)–(c) against the reference CHM, respectively. Similar performances can be observed for the *L*-band PD (i.e., $R^2 = 0.788$ and RMSE $=$ 1.802 m) and *X*-band HSPC (i.e., $R^2 = 0.744$ and RMSE $=$ 1.938 m). Although the accuracy of the difference between the *L*- and *X*-bands SPCs (i.e., $R^2 = 0.611$ and RMSE $= 2.042$ m) is not sufficiently high, as in the case of the *L*-band PD and *X*-band HSPC, this indicator can be used to determine the forest height without using the DTM and DSM. Findings in Figs. 5–8 proved

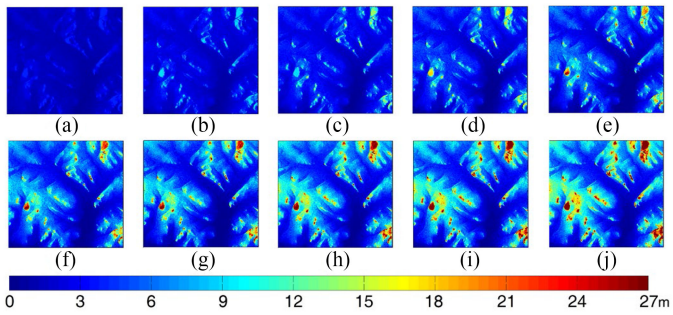

Fig. 9. RH difference for RRH10 to RRH100 extracted from the simulated *L*-band MB SAR data with a vertical resolution of 6.84 m [RH difference = RRH– min(RRH)]. (a) RRH10. (b) RRH20. (c) RRH30. (d) RRH40. (e) RRH50. (f) RRH60. (g) RRH70. (h) RRH80. (i) RRH90. (j) RRH100.

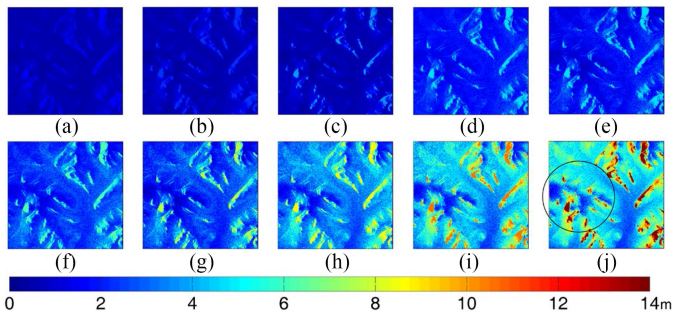

Fig. 10. RH difference for RRH10 to RRH100 extracted from the simulated *X*-band MB SAR data with a vertical resolution of 6.78 m [RH difference = RRH– min(RRH)]. (a) RRH10. (b) RRH20. (c) RRH30. (d) RRH40. (e) RRH50. (f) RRH60. (g) RRH70. (h) RRH80. (i) RRH90. (j) RRH100.

that the LandSAR can precisely simulate the TomoSAR features over mountainous areas.

B. Retrieved L- *and* X-*Bands RRH10 to RRH100*

Fig. 9 shows the RH difference of the extracted RRH10 to RRH100 from the simulated *L*-band MB SAR data, with a vertical resolution of 6.84 m [RH difference = RRH – min(RRH)]. The RH difference increases as the backscattered energy increases from 10% to 100%. Comparing the height values shown in Fig. 9(a) with those shown in Fig. 2(b), it can be noted that both the mountainous and flat areas exhibit similar height values in Fig. 9(a). The difference becomes more notable as the RRH increases. However, at a certain backscattered energy (i.e., approximately 50% or 60%), the corresponding height of the RRH between areas with high and low forest height stabilizes. This phenomenon may be interpreted considering Fig. 4; specifically, regardless of the areas with different forest height, the increased speed of the RRH becomes slow when a peak is identified in the profile.

Fig. 10 is the same as Fig. 9, but the RRH10 to RRH100 are extracted from the simulated *X*-band MB SAR data, with a vertical resolution of 6.78 m. Similar to the result in Fig. 9, the RRH increases as the backscattered energy increases from 10% to 100%. However, we observe some differences between Figs. 9 and 10. The range of the *X*-band RH difference (i.e., approximately 14 m) is less than that of the *L*-band RH difference (i.e., approximately 27 m), which can be interpreted by the limited penetration capability of the *X*-band, as shown in Fig. 5(e) and (f). The *X*-band penetration is influenced by the scatterer density, forest structure, and AGB [65]. A clearer penetration difference between *L*- and *X*-bands is observed in the areas with forest height greater than approximately 15 m, as pointed out by the black circle in Fig. 10(j).

Fig. 11 shows the correlation of the *L*-band RRH10 to RRH100 to the reference forest height. Fig. 11(a)– (j), respectively, shows the scattering plots of RRH10 to RRH100, derived from the simulated *L*-band MB SAR data, with a vertical resolution of 6.84 m, against the reference forest height. The RMSE increases with RRH enhancing. This can be attributed to a widened height range. In addition, the correlation of R^2 is distinctly enhanced as the RRH increases from 10% to 60%. However, the changes in the correlation stabilize when the RRH increases to more than 70%. These phenomena are consistent with the observations from Fig. 9. The highest performance corresponds to RRH90 (i.e., $R^2 = 0.712$), for the height range of approximately 8–33 m. Although the dynamic range of RRH100 is the largest, R^2 decreases slightly as the RRH increases from 90% to 100%. This can be explained by Fig. 4. The signal below the land surface is not the response of the vertical structure, which results in the reduction of R^2 between RRH100 and the reference forest height.

Fig. 12 shows the scattering plots of RRH10 to RRH100, derived from the simulated *X*-band MB SAR data, with a vertical resolution of 6.78 m, against the reference forest height. The correlations between forest height and *X*-band RRH10 to RRH100 are far below those between forest height and *L*-band RRH10 to RRH100. In addition, the influence of forest height on the penetration capability of the *X*-band is obviously found in Fig. 12. The *X*-bands RRH10 to RRH100 are negatively correlated with the forest height. This phenomenon can also be explained by the restricted penetration capability of the *X*-band. Generally, the penetration capability of the *X*-band in low forest height areas is stronger than that in the high forest height areas because a taller forest is usually of a more complicated canopy structure.

Fig. 13 demonstrates the correlation for the linear regression between the reference forest height and *L*-band RRH10 to RRH100 with the vertical resolutions ranging from 13.68 to 6.84 m. It can be noted that the observations in Fig. 11, for a vertical resolution of 6.84 m, are similar to those observed in this case, for the vertical resolutions of 13.68 to 7.46 m. Similar correlations are noted for all vertical resolutions, especially when the RRH exceeds 60%. This finding indicates that the RRH is not sensitive to the baseline distribution (or vertical resolution).

The correlations between the reference forest height and the combination of *L*-band RRH10 to RRH100, obtained using the stepwise linear regression for each vertical resolution, are presented in Table III. Similar correlations can be noted for each combined model. Moreover, the performance of the combined model is higher than that of the model regressed through a single

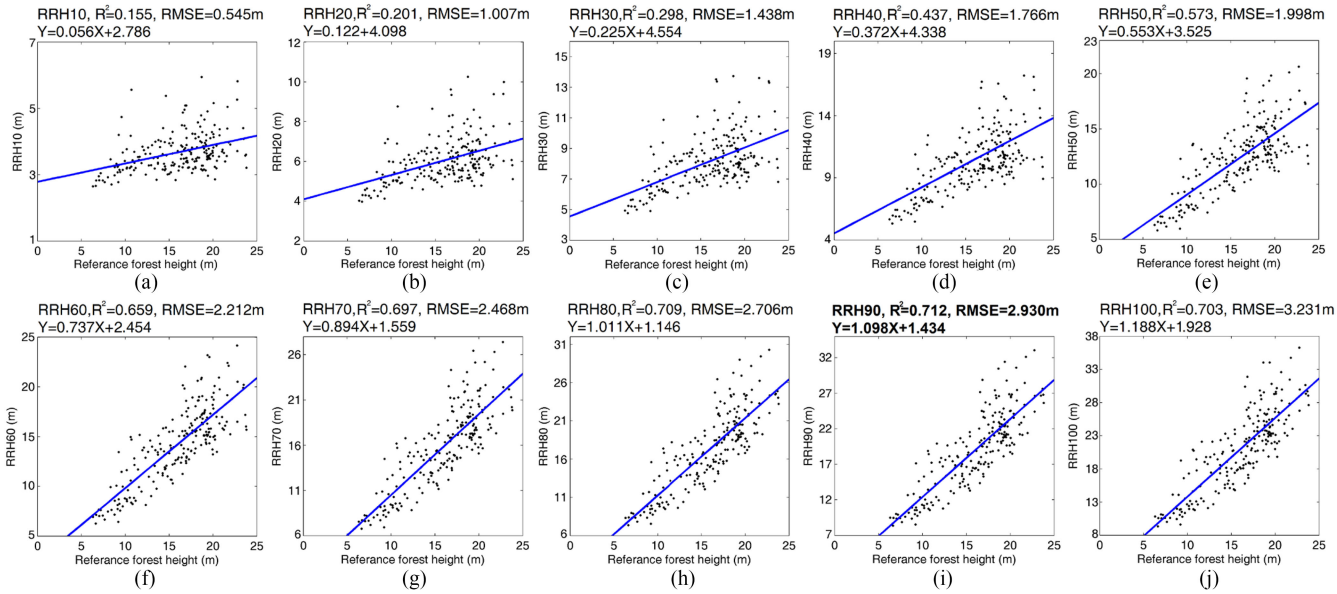

Fig. 11. Correlation of the *L*-band RRH10 to RRH100 with a vertical resolution of 6.84 m to the reference forest height. (a) RRH10. (b) RRH20. (c) RRH30. (d) RRH40. (e) RRH50. (f) RRH60. (g) RRH70. (h) RRH80. (i) RRH90. (j) RRH100. The blue lines are linear fitting lines for a given R^2 and the formula.

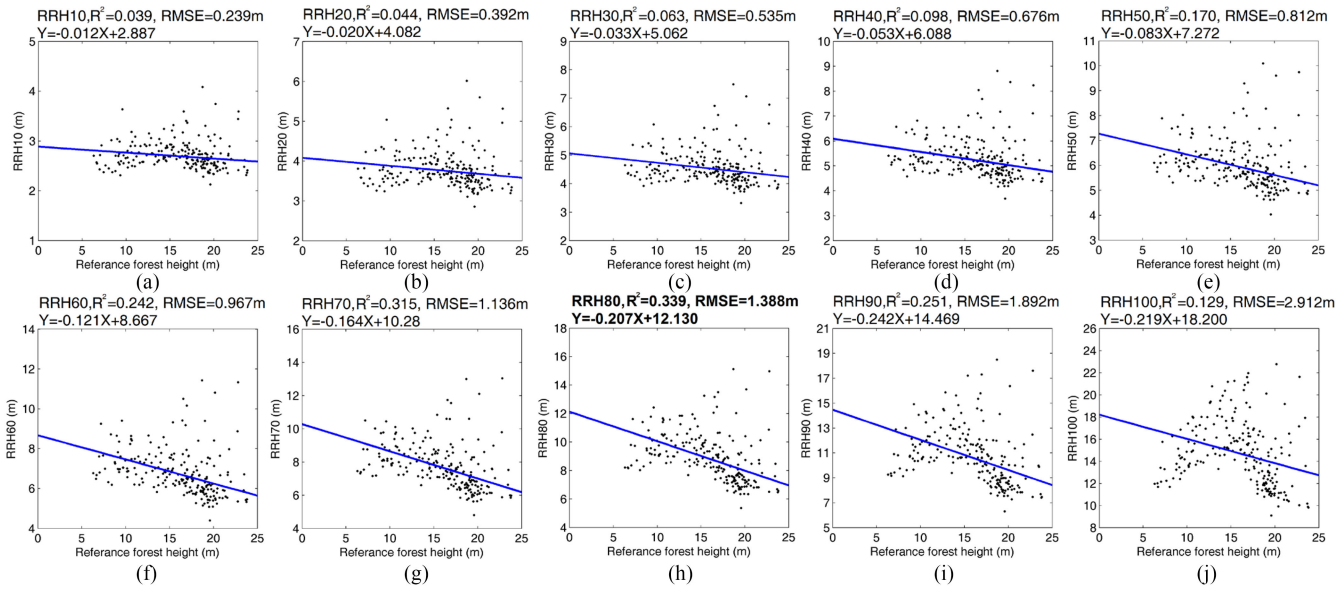

Fig. 12. Correlation of the *X*-band RRH10 to RRH100 with a vertical resolution of 6.78 m to the reference forest height. (a) RRH10. (b) RRH20. (c) RRH30. (d) RRH40. (e) RRH50. (f) RRH60. (g) RRH70. (h) RRH80. (i) RRH90. (j) RRH100. The blue lines are linear fitting lines for a given R^2 and the formula.

metric of RRH10 to RRH100. The highest correlation occurs under a vertical resolution of 6.84 m because the tomographic profiles with a higher vertical resolution contain more abundant structural information. In addition, for each vertical resolution, most of the ten metrics are excluded from the models, and only RRH10 and RRH90 are remained in the models. The metrics used for the model regression is derived from the forest canopy top (i.e., RRH10) and bottom (i.e., RRH90), indicating that redundancies are subsistent in the redefined metrics, and RRH10 and RRH90 are enough to describe the 3-D structure.

Interpretations for the selection of RRH10 to RRH100 in Table III are summarized as follows. As we can see from Fig. 4, RRH90 contains the two parts of height (or information), which is partly from the SSP to forest canopy top and partly from forest volume (i.e., forest canopy top to forest bottom). It can be expected that the retrieval accuracy should be enhanced ulteriorly if the height from the SSP to forest canopy top can be removed from RRH90 because the distribution of backscattered power from the SSP to forest canopy top is not caused by the 3-D canopy structure. With this in mind, we provide the

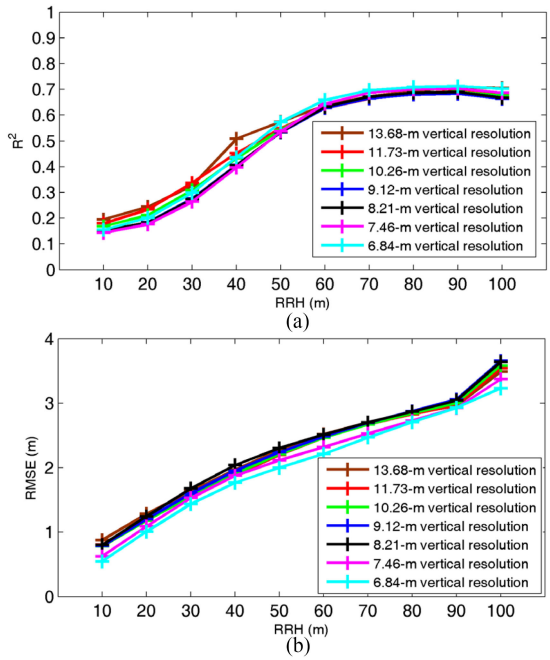

Fig. 13. Correlations between the reference forest height and *L*-band RRH10 to RRH100, with vertical resolutions ranging from 13.68 to 6.84 m, and a fixed HoA of 328.32 m. (a) R^2. (b) RMSE.

TABLE III
MODELS REGRESSED BY COMBINATION OF RRH10 TO RRH100 USING STEPWISE LINEAR REGRESSION UNDER DIFFERENT VERTICAL RESOLUTIONS

Vertical resolution (m)	Regression model formula [a]	R^2
13.68	H = -1.661RRH10 + 0.762RRH90 + 8.359	0.822
11.73	H = -1.493RRH10 + 0.797RRH90 + 8.522	0.834
10.26	H = -1.344RRH10 + 0.814RRH90 + 9.517	0.847
9.12	H = -1.535RRH10 + 0.825RRH90 + 10.869	0.841
8.21	H = -1.674RRH10 + 0.830RRH90 + 10.958	0.855
7.46	H = -1.814RRH10 + 0.862RRH90 + 9.787	0.843
6.84	H = -1.733RRH10 + 0.768RRH90 + 8.735	0.863

[a] *H* in the formulas indicates the forest height.

following explanations for the results: RRH10 mainly represents the information from the SSP to forest canopy top, and RRH10 and RRH90 are combined to obtain the height from the forest volume, which is then used to retrieve the forest height. This should be the reason that RRH10 and RRH90 have remained in all models. To validate the explanation mentioned above, we evaluate the sensitivity of forest height to the height difference between RRH90 and RRH10 to RRH80 using the sampling plots collected in Section III-B. The results are shown in Fig. 14. We observe that RRH90 – RRH10 obtains the highest correlation ($R^2 = 0.734$) with the forest height, which proves the rationality of our expiations.

The accuracy of the combined model with a vertical resolution of 6.84 m, as indicated in Table III, is illustrated in Fig. 15. Compared with the reference forest height, the R^2 and RMSE for the forest height predicted using the model regressed through the combination of RRH10 to RRH100 are 0.909 and 1.648 m,

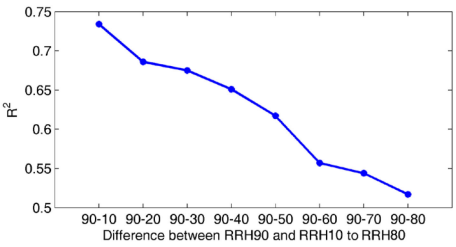

Fig. 14. Sensitivity of forest height to the height difference between RRH90 and RRH10 to RRH80 estimated from TomoSAR data with a vertical resolution of 6.84 m. "90-10" to "90-80" in the *x*-axis represent RRH90 - RRH10 to RRH90 - RRH80, respectively.

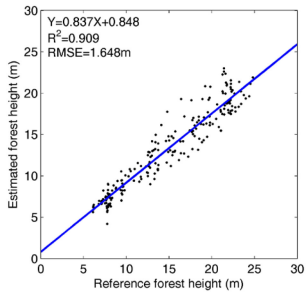

Fig. 15. Comparison between the reference forest height and estimated forest height when using the combined model indicated in Table III with a vertical resolution of 6.84 m. The blue line is the linear fitting line for a given R^2 and the formula.

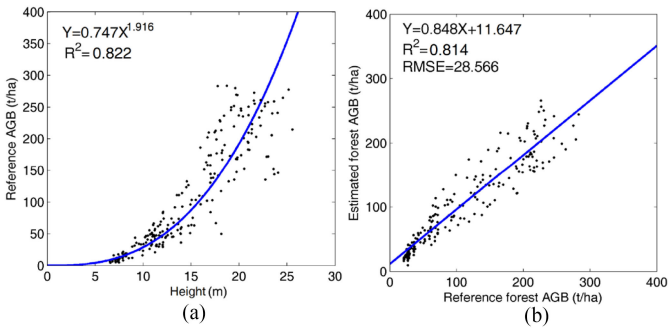

Fig. 16. (a) Height-to-biomass allometry regressed by the forest height and reference AGB. (b) Scatter plots of reference AGB against the estimated AGB using the equation derived in (a).

respectively, which indicates the considerable potential of the RRH metrics to retrieve the forest height from the *L*-band MB SAR data. In Fig. 16(a), the estimated forest height is plotted against the reference forest AGB. In Fig. 16(b), the predicted forest AGB using the regressed model in Fig. 16(a) is demonstrated. The predicted forest AGB correlates to the reference AGB with R^2 and RMSE of 0.814 and 28.566 t/ha, respectively. Such a high correlation is attributed to relatively homogeneous forest stand density in the study area. If the forest stand density is heterogeneous in other study areas, the use of height-to-biomass allometry to retrieve forest AGB may be restricted due to changeable forest stand densities. The forest height and AGB maps with a resolution of 15 × 15 m

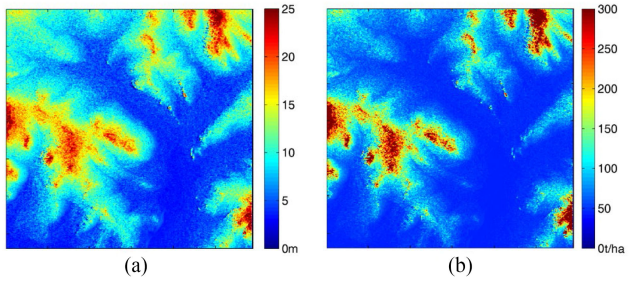

Fig. 17. (a) Forest height estimated by the combined model in Table III with a vertical resolution of 6.84 m. (b) Forest AGB using the estimated forest height and allometric equation.

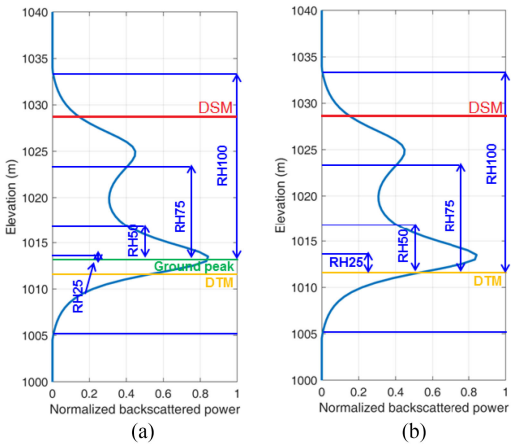

Fig. 18. Schematic view of the traditional RH metrics estimated by (a) first method (i.e., using the derived ground peak) and (b) second method (i.e., using the reference DTM).

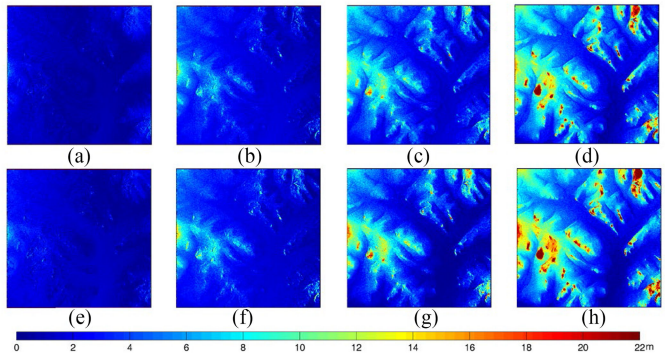

Fig. 19. RH difference of the traditional RH metrics (i.e., RH25, RH50, RH75, and RH100) derived from the simulated *L*-band MB SAR dataset with a vertical resolution of 6.84 m [RH difference = RH – min(RH)]. (a)–(d) are RH25, RH50, RH7,5 and RH100 estimated using the ground peak. (e)–(h) are RH25, RH50, RH75, and RH100 estimated using the reference DTM.

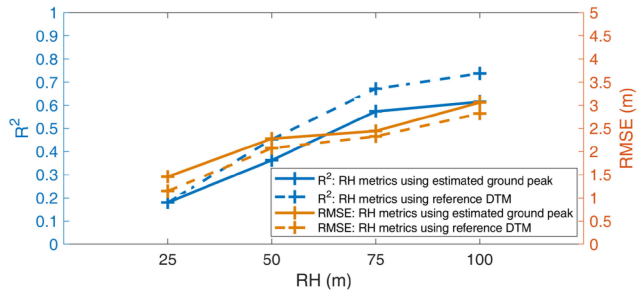

Fig. 20. Correlation between the reference forest height and the RH metrics derived from simulated *L*-band MB SAR dataset with a vertical resolution of 6.84 m. The blue and orange lines represent R^2 and RMSE, respectively. Solid and dotted lines indicate the RH metrics estimated using the ground peak and the reference DTM, respectively.

($\sim$ 0.2 ha) estimated by the combined model in Table III with a vertical resolution of 6.84 m are shown in Fig. 17, and they demonstrate a high level of agreement with the input CHM and reference forest AGB.

C. Influence of Ground Peak on Forest Height Estimation Using Traditional RH Metrics

Two ways are used to retrieve the traditional RH metrics in this study. The first method considers the lowest effective peak as the ground surface, as shown in Fig. 18(a), while the second method directly applies the reference DTM to derive the traditional RH metrics, as shown in Fig. 18(b). The accuracy of the elevation of the estimated ground peak is evaluated using the input DTM with a correlation of $R^2 = 0.984$ and RMSE = 2. 617 m. The influence of the ground peak on forest height estimation is analyzed by evaluating the sensitivity of reference forest height to RH metrics estimated by the two methods. It should be mentioned that both RRH metrics and traditional RH metrics are derived from the same vertical profiles with sidelobes removal using the method in Section IV-B.

The RH difference of the RH metrics (i.e., RH25, RH50, RH75, and RH100) derived from the simulated *L*-band MB SAR dataset using the two methods, with a vertical resolution of 6.84 m, are shown in Fig. 19 [RH difference = RH – min(RH)]. Fig. 19(a)–(d) and (e)–(h) is the results from the first and second methods, separately. Similar characteristics are observable in Figs. 9 and 19. The quantitative validation on the correlation between the reference forest height and RH metrics estimated using the two methods is shown in Fig. 20. For each percentage, RH metrics estimated using the reference DTM obtain the better performance than those estimated using the ground peak. The highest correlation is obtained by the *L*-band RH100 using the reference DTM with the R^2 of 0.737, which is similar to that of the *L*-band RRH90 ($R^2 = 0.712$) but higher than that of the *X*-band RRH80 ($R^2 = 0.339$). A more specific comparison for RH100 using the two methods is shown in Fig. 21. To better show their difference, all data are plotted in one picture. Obviously, the red points (i.e., RH100 using reference DTM) are more concentrated along the fitting line.

The model for the forest height estimation using the combination of *L*-band RH25 to RH100 with the stepwise linear regression can be expressed as

$$H = -0.028\mathrm{RH25} - 0.429\mathrm{RH50} + 0.709\mathrm{RH75} + 0.374\mathrm{RH100} + 3.863, R^2 = 0.738 \quad (10)$$

$$H = -0.065\mathrm{RH25} - 0.616\mathrm{RH50} + 0.737\mathrm{RH75} + 0.439\mathrm{RH100} + 5.397, R^2 = 0.877 \quad (11)$$

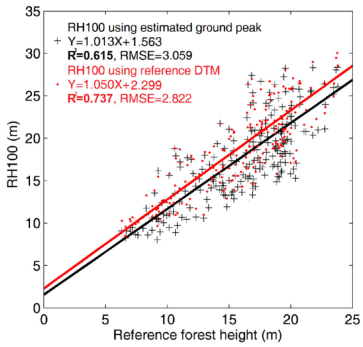

Fig. 21. Correlation of the *L*-band RH100 estimated using the ground peak (black cross) and the reference DTM (redpoint) with a vertical resolution of 6.84 m to the reference forest height. The blue and red lines are linear fitting lines for a given R^2 and the formula.

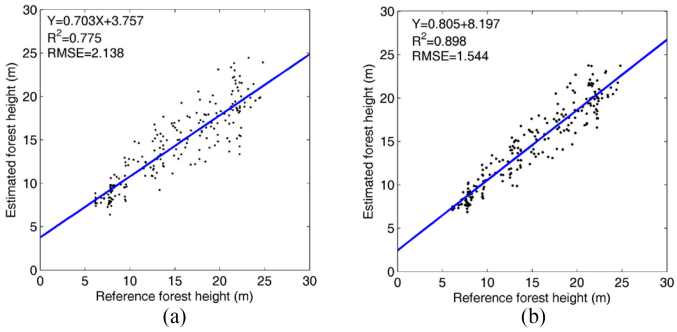

Fig. 22. Scatter plots of the predicted forest height by (a) model (10) and (b) model (11) against the reference forest height. The blue lines are linear fitting lines for a given R^2 and the formula.

where RH25 to RH100 in model (10) and model (11) are derived using the estimated ground peak and reference DTM, respectively. The traditional RH metrics can depict detailedly the canopy structure and all RH metrics remained in model (10) and model (11). The results indicate that the correlation for model (11) is close to those for the models in Table III and higher than that for model (10), but less redundant information is found in the traditional RH metrics. Fig. 22(a) and (b) demonstrates the scatter plot of the predicted forest height by model (10) and model (11) against the reference forest height, respectively. The results in Fig. 22 can be expected, the predicted forest height using the second method exhibits a higher correlation with the reference forest height, involving $R^2 = 0.898$ and RMSE $= 1.544$ m. The different performances of these two methods indicate that the error caused by the ground peak estimation is propagated to the forest height estimation when using the traditional RH metrics.

Figs. 19–22 prove that the redefined RH metrics obtain a similar performance to the traditional RH metrics estimated using the reference DTM. In addition, the traditional RH metrics can be used for the forest height estimation when the SSP and SEP are correctly defined and a high-accuracy DTM or accurate topography retrieval algorithm is used.

VI. Discussion

A. Influence of Capon Estimator on Height Estimation

The method used to derive the TomoSAR profiles is the Capon estimator. It should be noted that different tomographic algorithms provide different vertical profiles and all methods have their advantages and disadvantages. For example, the Fourier-based method is of good radiometric accuracy in the vertical direction while its vertical resolution is limited. The CS method or spectral estimators such as Capon and MUSIC are of abilities on super-resolution imaging and sidelobes suppression, but the radiometric accuracy is relatively poor. Because the development of the method, which can obtain radiometric accuracy and vertical resolution in the meantime is very challenging, especially under the circumstance of lacking accurate prior knowledge, the application of the Capon method can be regarded as a compromise. In addition, although the Capon estimator can lead to backscattered power bias in the vertical direction, the forest height estimation is performed by the vertical structure information from the waveform of the TomoSAR profile instead of the direct use of layered backscattered power. This may explain why a high correlation between the forest height and RH metrics is achieved in spite of using the Capon estimator.

B. Reason for Not Taking the SPC Point as the SEP

Although the signal below the land surface should be caused by the TomoSAR imaging method instead of the forest structure, the reason to not take the SPC point as the SEP is that the locations of the SPC point are changed in different areas. The location of the SPC is influenced by the scatterer density, 3-D canopy structure, and forest AGB. A clear example is shown in Fig. 5(b) and (c). We observe that most of the *L*-band SPCs are located along with the profile from the DTM due to the dominant double-bounce backscattering. However, few SPCs are located within the forest volume because of the influence of the scatterer density or forest AGB. For these pixels, the extraction of RRH10 to RRH100 is not suitable if we take the SPC point as the SEP.

C. Advantage and Disadvantage of the RRH Metrics

The comparison among the *L*-band RRH metrics, *X*-band RRH metrics, and *L*-band traditional RH metrics estimated using the reference DTM and identified ground peak on the forest height estimation is carried out in this study. The *L*-band RRH metrics and traditional RH metrics estimated using the reference DTM obtain similar performances. The correlation between the forest height and *L*-band traditional RH metrics estimated using the ground peak is lower than that between the forest height and *L*-band RH metrics estimated using the identified ground peak due to the estimation error on the ground surface. The *X*-band RRH metrics perform worst because of the limited penetration capability.

The influence of the baseline distribution and total baseline length on the retrieval of the forest height is discussed in this study. This is very critical because a reasonable baseline design can help to achieve a high vertical resolution and HoA. It is noted that the minimum baseline interval does not considerably change

the waveform of the vertical profile, while the total baseline length significantly transforms the waveform due to different vertical resolutions. Moreover, the correlation between the reference height and *L*-band RRH10 to RRH100 with different total baseline lengths is compared. Similar correlations were obtained until a certain RRH. These findings demonstrate that the redefined metrics are insensitive to the minimum baseline interval and total baseline length, thereby indicating that the redefined metrics can employ spare observations to realize accurate forest height estimation.

The disadvantage is that the RRH metrics are validated using the simulated MB SAR data. Using LandSAR, we can evaluate the influence of the change in a single parameter separated from other influences. This is generally difficult to accomplish using the actual SAR data. The capability of the LandSAR model for MB SAR data simulation has been verified by Ni *et al*. [35]. This article examines the profiles from the simulated TomoSAR data in three ways. The first way is to compare the estimated vertical profiles with profiles from the LiDAR DTM and reference DSM. The second way is to analyze the influence of the baseline distribution on the estimation of the vertical profiles. The third way is to evaluate the relationship between the reference CHM (reference CHM = input DSM-input DTM) and SPC-retrieved indicators, as shown in Fig. 8. The comparison between the input of LandSAR (i.e., the input DSM and input DTM) and SPC indicators retrieved from the simulated TomoSAR data is a common method to quantitatively evaluate the simulated results as did in [35], [45], and [51]. The *L*-band PD and *X*-band HSPC exhibit a good correlation with the reference CHM. The above-mentioned phenomena are all consistent with theoretical expectations. Therefore, we believe that the LandSAR model can be used to accurately simulate the spaceborne TomoSAR data. Note that a quantitative evaluation of the simulated data using the real spaceborne TomoSAR data is very important. However, the acquisition of the spaceborne TomoSAR data is rather difficult at this stage due to the temporal decorrelation. Estimating the vertical profile from the real spaceborne MB SAR data under the condition of temporal decorrelation is still a challenging topic and needs more experiments. Accordingly, the LandSAR will be examined using the spaceborne data from future SAR sensors (such as ESA BIOMASS) in future work.

In the comparison between *L*- and *X*-bands RRH metrics (i.e., as shown in Figs. 9–12), we can conclude that RH metrics are indeed required for a meaningful correlation with forest height, that is, the backscattered power distributed between the forest canopy top and ground surface is necessary. Low frequencies microwave can penetrate the forest canopy and reach the ground, therefore, a vertical profile within the range of the canopy top to the ground surface is certainly existing. However, for the high frequencies (such as *X*-band) TomoSAR data, the use of RH metrics on the forest height estimation is limited due to restricted penetration capability, as shown in Fig. 5(f). No backscattered power is distributed near the ground surface in the *X*-band vertical profile for areas with tall forests, and this phenomenon is also noted by Khati *et al*. [3], which demonstrates a study on the Indian tropical forests using the *X*-band TomoSAR data. Therefore, RH and RRH metrics are only suitable for forest height retrieval with low frequencies TomoSAR data.

VII. Conclusion

In this study, we first examined the performance of LandSAR in simulating the TomoSAR features. The Capon spectral analysis method was used to estimate the vertical profile. The results demonstrated that LandSAR can clearly model the tomographic characteristics. The distribution of the *L*- and *X*-band tomographic profiles in the forested areas exhibited a significant correlation with the reference DSM and LiDAR DTM. Next, the vertical profiles derived from different vertical resolutions and HoAs were compared. The HoA did not considerably influence the vertical profiles, while the vertical resolution strongly affected the waveform of the profiles. Subsequently, the RH metrics were redefined to estimate the forest height, which was then used to retrieve the forest AGB with a height-to-biomass allometry. The performances of the *L*- and *X*-bands RRH metrics and the *L*-band traditional RH metrics estimated using the reference DTM and identified ground peak on the forest height estimation were compared. The combination of the *L*-band RRH10 to RRH100 demonstrated a high correlation with the reference forest height, with a correlation of $R^2 = 0.863$ under a vertical resolution of 6.84 m. The R^2 and RMSE of the forest height estimated using the combined model were 0.909 and 1.648 m, respectively, compared with the reference forest height. Finally, the influence of different vertical resolutions on the forest height estimation was examined. Similar correlations were obtained with different vertical resolutions until a certain RRH, indicating the robustness of the RRH metrics. These results illustrate the capability of the TomoSAR techniques with the RRH metrics using the *L*-band MB SAR data to estimate the forest height and AGB. The performance of the RRH metrics will be further evaluated in future work, using actual spaceborne SAR data.

Acknowledgment

The authors would like to thank Prof. W. Ni for providing LandSAR, which was used to evaluate the RRH metrics.

References

[1] T. L. Toan, A. Beaudoin, J. Riom, and D. Guyon, "Relating forest biomass to SAR data," *IEEE Trans. Geosci. Remote Sens.*, vol. 30, no. 2, pp. 403–411, Mar. 1992.

[2] S. Englhart, V. Keuck, and F. Siegert, "Aboveground biomass retrieval in tropical forests—The potential of combined X- and L-band SAR data use," *Remote Sens. Environ.*, vol. 115, no. 5, pp. 1260–1271, 2011.

[3] U. Khati, M. Lavalle, and G. Singh, "Spaceborne tomography of multi-species Indian tropical forests," *Remote Sens. Environ.*, vol. 229, pp. 193–212, Aug. 2019.

[4] S. Quegan, T. L. Toan, J. J. Yu, F. Ribbes, and N. Floury, "Multitemporal ERS SAR analysis applied to forest mapping," *IEEE Trans. Geosci. Remote Sens.*, vol. 38, no. 2, pp. 741–753, Mar. 2000.

[5] C. T. de Almeida *et al.*, "Combining LiDAR and hyperspectral data for aboveground biomass modeling in the Brazilian amazon using different regression algorithms," *Remote Sens. Environ.*, vol. 232, Oct. 2019, Art. no. 111323.

[6] A. Reigber and A. Moreira, "First demonstration of airborne SAR tomography using multibaseline L-band data," *IEEE Trans. Geosci. Remote Sens.*, vol. 38, no. 5, pp. 2142–2152, Sep. 2000.

[7] M. Shahzad and X. X. Zhu, "Robust reconstruction of building facades for large areas using spaceborne TomoSAR point clouds," *IEEE Trans. Geosci. Remote Sens.*, vol. 53, no. 2, pp. 752–769, Feb. 2015.

[8] M. Shahzad and X. X. Zhu, "Automatic detection and reconstruction of 2-D/3-D building shapes from spaceborne TomoSAR point clouds," *IEEE Trans. Geosci. Remote Sens.*, vol. 54, no. 3, pp. 1292–1310, Mar. 2016.

[9] P. Ma, H. Lin, H. Lan, and F. Chen, "Multi-dimensional SAR tomography for monitoring the deformation of newly built concrete buildings," *ISPRS J. Photogrammetry Remote Sens.*, vol. 106, pp. 118–128, 2015.

[10] D. Liu *et al.*, "Evaluation of InSAR and TomoSAR for monitoring deformations caused by mining in a mountainous area with high resolution satellite-based SAR," *Remote Sens.*, vol. 6, no. 2, pp. 1476–1495, 2014.

[11] M. M. d'Alessandro and S. Tebaldini, "Retrieval of terrain topography in tropical forests using P-band SAR tomography," in *Proc. IEEE Int. Geosci. Remote Sens. Symp.*, 2018, pp. 8598–8600.

[12] M. M. d'Alessandro and S. Tebaldini, "Digital terrain model retrieval in tropical forests through P-band SAR tomography," *IEEE Trans. Geosci. Remote Sens.*, vol. 57, no. 9, pp. 6774–6781, Sep. 2019.

[13] M. Pardini and K. Papathanassiou, "Sub-canopy topography estimation: Experiments with multibaseline SAR data at L-band," in *Proc. IEEE Int. Geosci. Remote Sens. Symp.*, 2012, pp. 4954–4957.

[14] O. D'Hondt, R. Hansch, and O. Hellwich, "Feature design for classification from TomoSAR data," in *Proc. IEEE Int. Geosci. Remote Sens. Symp.*, 2018, pp. 6739–6742.

[15] O. D'Hondt, R. Hansch, N. Wagener, and O. Hellwich, "Exploiting SAR tomography for supervised land-cover classification," *Remote Sens.*, vol. 10, no. 11, pp. 1742–1759, Nov. 2018.

[16] S. Quegan *et al.*, "The European space agency BIOMASS mission: Measuring forest above-ground biomass from space," *Remote Sens. Environ.*, vol. 227, pp. 44–60, Jun. 15, 2019.

[17] P. C. Dubois-Fernandez *et al.*, "The TropiSAR airborne campaign in French Guiana: Objectives, description, and observed temporal behavior of the backscatter signal," *IEEE Trans. Geosci. Remote Sens.*, vol. 50, no. 8, pp. 3228–3241, Aug. 2012.

[18] D. H. T. Minh, T. L. Toan, F. Rocca, S. Tebaldini, M. M. d'Alessandro, and L. Villard, "Relating P-band synthetic aperture radar tomography to tropical forest biomass," *IEEE Trans. Geosci. Remote Sens.*, vol. 52, no. 2, pp. 967–979, Feb. 2014.

[19] D. H. T. Minh *et al.*, "SAR tomography for the retrieval of forest biomass and height: Cross-validation at two tropical forest sites in French Guiana," *Remote Sens. Environ.*, vol. 175, pp. 138–147, Mar. 15, 2016.

[20] S. Tebaldini, D. H. T. Minh, M. M. d'Alessandro, L. Villard, T. L. Toan, and J. Chave, "The status of technologies to measure forest biomass and structural properties: State-of-the-art in SAR tomography of tropical forests," *Surv. Geophys.*, vol. 40, pp. 779–801, 2019.

[21] W. Li, E. Chen, Z. Li, W. Zhang, and C. Jiang, "Assessing performance of tomo-SAR and backscattering coefficient for hemi-boreal forest above-ground biomass estimation," *J. Indian Soc. Remote Sens.*, vol. 44, no. 1, pp. 41–48, 2016.

[22] E. Blomberg, L. Ferro-Famil, M. J. Soja, L. M. Ulander, and S. Tebaldini, "Forest biomass retrieval from L-band SAR using tomographic ground backscatter removal," *IEEE Geosci. Remote Sens. Lett.*, vol. 15, no. 7, pp. 1030–1034, Jul. 2018.

[23] S. Tebaldini and F. Rocca, "Multibaseline polarimetric SAR tomography of a boreal forest at P- and L-bands," *IEEE Trans. Geosci. Remote Sens.*, vol. 50, no. 1, pp. 232–246, Jan. 2012.

[24] A. T. Caicoya, M. Pardini, I. Hajnsek, and K. Papathanassiou, "Forest above-ground biomass estimation from vertical reflectivity profiles at L-band," *IEEE Geosci. Remote Sens. Lett.*, vol. 12, no. 12, pp. 2379–2383, Dec. 2015.

[25] I. E. Moussawi *et al.*, "L-band UAVSAR tomographic imaging in dense forests: Gabon forests," *Remote Sens.*, vol. 11, no. 5, pp. 475–491, Feb. 2019.

[26] M. Pardini, M. Tello, V. Cazcarra-Bes, K. P. Papathanassiou, and I. Hajnsek, "L- and P-band 3-D SAR reflectivity profiles versus Lidar waveforms: The AfriSAR case," *IEEE J. Sel. Topics Appl. Earth Observ. Remote Sens.*, vol. 11, no. 10, pp. 3386–3401, Oct. 2018.

[27] Q. Chen, "Retrieving vegetation height of forests and woodlands over mountainous areas in the pacific coast region using satellite laser altimetry," *Remote Sens. Environ.*, vol. 114, no. 7, pp. 1610–1627, Jul. 15, 2010.

[28] R. O. Dubayah *et al.*, "Estimation of tropical forest height and biomass dynamics using lidar remote sensing at La Selva, Costa Rica," *J. Geophys. Res., Biogeosci.*, vol. 115, pp. 9–25, Jun. 2010.

[29] M. A. Hofton, J. B. Minster, and J. B. Blair, "Decomposition of laser altimeter waveforms," *IEEE Trans. Geosci. Remote Sens.*, vol. 38, no. 4, pp. 1989–1996, Jul. 2000.

[30] J. A. B. Rosette, P. R. J. North, and J. C. Suarez, "Vegetation height estimates for a mixed temperate forest using satellite laser altimetry," *Int. J. Remote Sens.*, vol. 29, no. 5, pp. 1475–1493, Feb. 2008.

[31] S. Lee, W. Ni-Meister, W. Z. Yang, and Q. Chen, "Physically based vertical vegetation structure retrieval from ICESat data: Validation using LVIS in white mountain national forest, New Hampshire, USA," *Remote Sens. Environ.*, vol. 115, no. 11, pp. 2776–2785, Nov. 15, 2011.

[32] V. Cazcarra-Bes, M. Pardini, M. Tello, and K. P. Papathanassiou, "Comparison of tomographic SAR reflectivity reconstruction algorithms for forest applications at L-band," *IEEE Trans. Geosci. Remote Sens.*, vol. 58, no. 1, pp. 147–164, Jan. 2020.

[33] X. Li, L. Liang, H. Guo, and Y. Huang, "Compressive sensing for multi-baseline polarimetric SAR tomography of forested areas," *IEEE Trans. Geosci. Remote Sens.*, vol. 54, no. 1, pp. 153–166, Jan. 2016.

[34] Y. Wang, W. Ni, G. Sun, H. Chi, Z. Zhang, and Z. Guo, "Slope-adaptive waveform metrics of large footprint lidar for estimation of forest aboveground biomass," *Remote Sens. Environ.*, vol. 224, pp. 386–400, Apr. 2019.

[35] W. Ni, Z. Zhang, G. Sun, and Q. Liu, "Modeling interferometric SAR features of forest canopies over mountainous area at landscape scales," *IEEE Trans. Geosci. Remote Sens.*, vol. 56, no. 5, pp. 2958–2967, May 2018.

[36] F. Lombardini and F. Cai, "Temporal decorrelation-robust SAR tomography," *IEEE Trans. Geosci. Remote Sens.*, vol. 52, no. 9, pp. 5412–5421, Sep. 2014.

[37] H. Aghababaee, G. Ferraioli, and G. Schirinzi, "Polarization analysis of the impact of temporal decorrelation in synthetic aperture radar (SAR) tomography," *Remote Sens.*, vol. 11, no. 6, pp. 686–699, 2019.

[38] A. Hamadi, L. Villard, P. Borderies, C. Albinet, T. Koleck, and T. L. Toan, "Comparative analysis of temporal decorrelation at P-band and low L-band frequencies using a tower-based scatterometer over a tropical forest," *IEEE Geosci. Remote Sens. Lett.*, vol. 14, no. 11, pp. 1918–1922, Nov. 2017.

[39] J. A. Richards, G.-Q. Sun, and D. S. Simonett, "L-band radar backscatter modeling of forest stands," *IEEE Trans. Geosci. Remote Sens.*, vol. 25, no. 4, pp. 487–498, Jul. 1987.

[40] G. Sun, D. S. Simonett, and A. H. Strahler, "A radar backscatter model for discontinuous coniferous forests," *IEEE Trans. Geosci. Remote Sens.*, vol. 29, no. 4, pp. 639–650, Jul. 1991.

[41] Y. Wang, J. Day, and G. Sun, "Santa Barbara microwave backscattering model for woodlands," *Int. J. Remote Sens.*, vol. 14, no. 8, pp. 1477–1493, May 20, 1993.

[42] Y. Wang, J. L. Day, F. W. Davis, and J. M. Melack, "Modeling L-band radar backscatter of Alaskan boreal forest," *IEEE Trans. Geosci. Remote Sens.*, vol. 31, no. 6, pp. 1146–1154, Nov. 1993.

[43] G. Sun and K. J. Ranson, "A three-dimensional radar backscatter model of forest canopies," *IEEE Trans. Geosci. Remote Sens.*, vol. 33, no. 2, pp. 372–382, Mar. 1995.

[44] W. Ni, Z. Guo, and G. Sun, "Improvement of a 3D radar backscattering model using matrix-doubling method," *Sci. China Earth Sci.*, vol. 53, no. 7, pp. 1029–1035, Jul. 2010.

[45] W. Ni *et al.*, "Model-based analysis of the influence of forest structures on the scattering phase center at L-band," *IEEE Trans. Geosci. Remote Sens.*, vol. 52, no. 7, pp. 3937–3946, Jul. 2014.

[46] E. R. Schmerling, R. Goerss, S. Miluschewa, P. Hertzler, and I. Pikus, "Ray tracing for whistler-mode signals at low frequencies," *Proc. Inst. Radio Engineers*, vol. 48, no. 3, pp. 408–408, 1960.

[47] F. T. Ulaby, K. Sarabandi, K. Mcdonald, M. Whitt, and M. C. Dobson, "Michigan microwave canopy scattering model," *Int. J. Remote Sens.*, vol. 11, no. 7, pp. 1223–1253, Jul. 1990.

[48] L. Tsang, C.-T. Chen, A. T. C. Chang, J. J. Guo, and K.-H. Ding, "Dense media radiative transfer theory based on quasicrystalline approximation with applications to passive microwave remote sensing of snow," *Radio Sci.*, vol. 35, no. 3, pp. 731–749, May/Jun. 2000.

[49] M. A. Karam, A. K. Fung, and Y. M. M. Antar, "Electromagnetic wave scattering from some vegetation samples," *IEEE Trans. Geosci. Remote Sens.*, vol. 26, no. 6, pp. 799–808, Nov. 1988.

[50] K. S. Chen, L. Tsang, J. C. Shi, and H. C. Huang, "Microwave emission from two-dimensional inhomogeneous dielectric rough surfaces based on physics-based two-grid method," *Prog. Electromagn. Res.*, vol. 67, pp. 181–203, 2007.

[51] D. Liu, G. Sun, Z. Guo, K. J. Ranson, and Y. Du, "Three-dimensional coherent radar backscatter model and simulations of scattering phase center of forest canopies," *IEEE Trans. Geosci. Remote Sens.*, vol. 48, no. 1, pp. 349–357, Jan. 2010.
[52] T. Zeng, C. Hu, H. Sun, and E. Chen, "A novel rapid SAR simulator based on equivalent scatterers for three-dimensional forest canopies," *IEEE Trans. Geosci. Remote Sens.*, vol. 52, no. 9, pp. 5243–5255, Sep. 2014.
[53] K. Sarabandi and Y.-C. Lin, "Simulation of interferometric SAR response for characterizing the scattering phase center statistics of forest canopies," *IEEE Trans. Geosci. Remote Sens.*, vol. 38, no. 1, pp. 115–125, Jan. 2000.
[54] L. Thirion, E. Colin, and C. Dahon, "Capabilities of a forest coherent scattering model applied to radiometry, interferometry, and polarimetry at P- and L-band," *IEEE Trans. Geosci. Remote Sens.*, vol. 44, no. 4, pp. 849–862, Apr. 2006.
[55] Y.-C. Lin and K. Sarabandi, "A Monte Carlo coherent scattering model for forest canopies using fractal-generated trees," *IEEE Trans. Geosci. Remote Sens.*, vol. 37, no. 1, pp. 440–451, Jan. 1999.
[56] K. K. Tse, L. Tsang, C. H. Chan, K. H. Ding, and K. W. Leung, "Multiple scattering of waves by dense random distributions of sticky particles for applications in microwave scattering by terrestrial snow," *Radio Sci.*, vol. 42, no. 5, pp. 1–14, Oct. 2007.
[57] Y. Pang, Z. Li, K. Zhao, E. Chen, and G. Sun, "Temperate forest aboveground biomass estimation by means of multi-sensor fusion: The Daxinganling campaign," in *Proc. IEEE Int. Geosci. Remote Sens. Symp.*, 2013, pp. 991–994.
[58] W. Li, Q. Guo, M. K. Jakubowski, and M. Kelly, "A new method for segmenting individual trees from the lidar point cloud," *Photogrammetric Eng. Remote Sens.*, vol. 78, no. 1, pp. 75–84, Jan. 2012.
[59] D. L. Urban, G. B. Bonan, T. M. Smith, and H. H. Shugart, "Spatial applications of gap models," *Forest Ecol. Manage.*, vol. 42, no. 1/2, pp. 95–110, 1991.
[60] J. Capon, "High-resolution frequency-wavenumber spectrum analysis," *Proc. IEEE*, vol. 57, no. 8, pp. 1408–1418, Aug. 1969.
[61] M. Pardini and K. Papathanassiou, "On the estimation of ground and volume polarimetric covariances in forest scenarios with SAR tomography," *IEEE Geosci. Remote Sens. Lett.*, vol. 14, no. 10, pp. 1860–1864, Oct. 2017.
[62] A. T. Caicoya, F. Kugler, M. Pardini, I. Hajnsek, and K. Papathanassiou, "Vertical forest structure characterization for the estimation of above ground biomass: First experimental results using SAR vertical reflectivity profiles," in *Proc. IEEE Int. Geosci. Remote Sens. Symp.*, 2014, pp. 1045–1048.
[63] A. T. Caicoya, F. Kugler, H. Pretzsch, and K. Papathanassiou, "Forest vertical structure characterization using ground inventory data for the estimation of forest aboveground biomass," *Can. J. Forest Res.*, vol. 46, no. 1, pp. 25–38, Jan. 2016.
[64] K. P. Papathanassiou and S. R. Cloude, "Single-baseline polarimetric SAR interferometry," *IEEE Trans. Geosci. Remote Sens.*, vol. 39, no. 11, pp. 2352–2363, Nov. 2001.
[65] F. Kugler, D. Schulze, I. Hajnsek, H. Pretzsch, and K. P. Papathanassiou, "TanDEM-X Pol-InSAR performance for forest height estimation," *IEEE Trans. Geosci. Remote Sens.*, vol. 52, no. 10, pp. 6404–6422, Oct. 2014.

Haoyang Yu received the B.S. degree from the College of Mechanical and Electronic Engineering, Shandong Agricultural University, China, in 2014. He is currently pursuing the Ph.D. degree at the Beijing Normal University.

His main research interest concerns use of SAR data for forest and non-forest classification, multi-temporal SAR data analysis, SAR data simulation, and application of SAR remote sensing for the retrieval of forest bio-physical parameters.

Zhongjun Zhang received the B.Sc. degree in electronics, the M.Sc. degree in signal processing, and the Ph.D. degree in remote sensing and GIS from Beijing Normal University (BNU), Beijing, China, in 1990, 1999, and 2004, respectively.

He was a Visiting Scientist at the Hydrology and Remote Sensing Laboratory, U.S. Department of Agriculture, Washington, DC, USA, in 2006. He was a Visiting Scholar with The City University of New York, New York, NY, USA, in 2015. He is currently a Professor with the School of Artificial Intelligence, BNU. His research interests are microwave remote sensing and image processing.